

Particle in cell calculation of plasma force on a small grain in a non-uniform collisional sheath

I H Hutchinson

Plasma Science and Fusion Center and
Department of Nuclear Science and Engineering,
Massachusetts Institute of Technology,
Cambridge, MA, USA

Abstract

The plasma force on grains of specified charge and height in a collisional DC plasma sheath are calculated using the multidimensional particle in cell code COPTIC. The background ion velocity distribution functions for the unperturbed sheath vary substantially with collisionality. The grain force is found to agree quite well with a combination of background electric field force plus ion drag force. However, the drag force must take account of the non-Maxwellian (and spatially varying) ion distribution function, and the collisional drag enhancement. It is shown how to translate the dimensionless results into practical equilibrium including other forces such as gravity.

1 Introduction

Many dusty plasma phenomena are associated with the suspension of dust grains near the edge of a sheath formed between the plasma and a wall, e.g.[1, 2, 3, 4]. The grains therefore reside in an inherently non-uniform plasma environment, and the scale length of non-uniformity is generally comparable to that of the shielded grain potential. The “plasma” forces on the grain consist of the ion drag arising from the ion flow into the wall-sheath, and the electric field force from the sheath potential gradient. In addition, gravity and other forces such as neutral drag or thermophoretic force may need to be considered, but they are not the object of the present calculations. The ion drag force is the quantity least well established. The present work is devoted to calculating by direct particle in cell (PIC) simulation the total plasma force including the ion drag on a grain in a self-consistent sheath. The results provide quantitative theoretical total plasma force values and establish the extent to which the inherent non-uniformity affects the result, by comparing the force with that derived from formulas for ion drag force in *uniform* plasmas.

The physics of a collisional sheath is well established [5, 6] and the non-linear kinetic equations have been solved [7, 8, 9] in one dimension. To calculate the drag force on a grain by simulation, however, requires a multidimensional calculation, because the drag arises from

the nearby perturbation of the plasma. A grain finite in the transverse dimensions breaks the one-dimensional symmetry. At least two-dimensions in space are required and three in velocity. In fact the present work is performed using a code that is three-dimensional in space, COPTIC[10]. The extra computational effort of an additional dimension, while significant, is partly recouped by the averaging inherent in obtaining the longitudinal force. A fully three-dimensional code is required to explore the interaction of multiple grains, for which COPTIC is fully equipped[11], but that endeavor will not be undertaken here.

The organization of the paper is that section 2 describes the methods of calculation in the context of the bare, one-dimensional sheath, which provides the background plasma in which the grain is to be placed. Three different levels of collisionality are explored. Section 3 explains how the force on the grain is expressed and calculated, and gives the numerical results for a range of grain charge and height in the sheath. Then section 4 compares these results with what would be predicted by combining the electric field force and the theoretical ion drag force for a *uniform* plasma having parameters equal to their local values in the non-uniform sheath. The discussion section illustrates the application to a characteristic experimental situation.

2 Collisional Sheath

The first requirement of an accurate theoretical calculation of grain force in a sheath is an accurate representation of the sheath. Strictly speaking, the interest is in the regions spanning the sheath and the presheath, where the plasma makes a transition from the quasineutral presheath (or some would say simply the “plasma”) into the region of non-negligible charge density that is the sheath. It is well known that a slab-geometry non-uniform presheath cannot exist without particle, momentum, or energy sources in the presheath[7, 12, 5]. They arise from collisions.

In this paper we exclude ionization, which may be important in many physical situations. We also ignore the possibility of strong neutral density gradients or flow arising from recycling and atomic processes close to the wall. We allow only for charge-exchange ion collisions with a uniform, stationary, background neutral gas. They are quite well represented by a Bhatnagar, Gross and Krook (BGK) type of collision term. The collisions are therefore substantially idealized. A collision consists of replacing the colliding ion with a new one having velocity drawn from the neutral atom distribution function. Although the charge exchange cross-section for commonly used gases is not exactly inversely proportional to inter-particle speed, it is a reasonable approximation to take the collision frequency to be independent of speed. This approximation produces substantial simplifications, such as making the background solution of the Boltzmann equation separable, but does not represent precisely the collisional atomic physics. The neutral distribution is here taken to be a stationary Maxwellian with temperature T_n .

Moderate collisionality. The form of the presheath/sheath structure is illustrated in Fig. 1. Four quantities are plotted: the electron and ion densities n_e and n_i , the electric potential ϕ and the ion fluid (average) velocity, v_f , all as a function of distance z from the wall. All quantities are expressed in normalized units defined with respect to the reference position

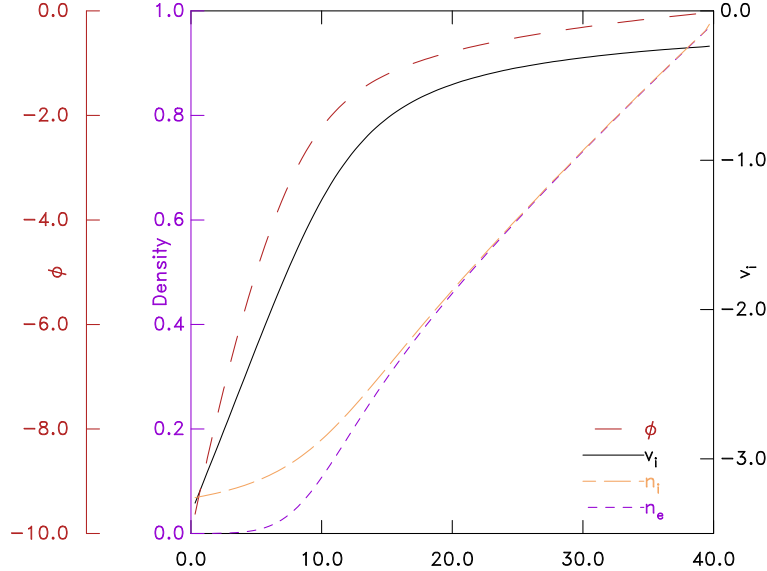


Figure 1: Collisional sheath spatial structure for collision time $\tau_c = 10$. Spatial distances are in units of the electron Debye length at the reference position, $z = 40$. The wall is at $z = 0$. All quantities are in normalized units, with v_i denoting the fluid ion flow speed (v_f).

$z = 40$. The units of z are electron Debye lengths $\lambda_{De} = \sqrt{\epsilon_0 T_e / n_{e40} e^2}$, and of potential are T_e/e , where T_e is the assumed uniform electron temperature. The units of velocity are the cold-ion sound speed $c_s = \sqrt{T_e/m_i}$, and the densities are normalized to the reference density. Collisions occur at a rate defined by a collision time τ_c expressed in units of λ_{De}/c_s . Therefore, the value $\tau_c = 10$ makes the mean free path at speed c_s equal to 10 (normalized space units), a quarter of the space range plotted. We will consider only $T_n = 0.02T_e$ in this paper.

The general character is that, starting from a distant position in the presheath at the right, the density decreases towards the wall. The potential and the electron density are presumed to be governed by a Boltzmann relationship:

$$n_e(\phi) = n_{e40} \exp(e\phi/T_e), \quad (1)$$

or in normalized units $n_e = \exp(\phi)$. This approximation not significantly affected by electron loss (cutting off the distribution) far from the wall, because virtually all electrons there are reflected. Although distribution cut-off compromises its accuracy close to the wall, the inaccuracy does not matter because the electron density is negligible there anyway. As the potential drops, the ions accelerate from subsonic speed. As they approach the sound speed $v_f = -1$, quasi-neutrality breaks down and the electron and ion densities begin to differ, and non-negligible positive charge density is present. This is the entrance into the sheath. In the sheath the potential falls more steeply, soon reducing the electron density to a negligible level, while the ions continue to accelerate to supersonic speeds through the potential gradient.

The wall in these calculations is considered to be held at a constant (negative) potential $\phi = -10$, and the relevant solution is steady. This formally represents a DC sheath. RF sheaths are frequently of practical significance and have been studied in the context of dust

levitation both analytically[13] and computationally[14]. They act approximately like a DC sheath with the ions feeling the time-averaged potential, but with the average electron current to the wall adjustable by the amplitude of the RF component of the potential. Consequently RF sheaths can experience controllable, and sometimes quite negative, wall potentials. Although RF modulation of atomic excitation is observed in experiments, this is attributed mostly to energetic electrons; and the grain charge is barely modulated[15]. The simulation ignores all modulation and effectively considers the wall potential to be controllable. If that potential is made more negative, all that happens is that the solution shape remains unchanged but it moves horizontally toward the right. Therefore a single simulation is sufficient to represent virtually any wall potential provided we do not wish to explore positions closer to the wall.

Figure 1 is the result of an actual Particle in Cell calculation using the code COPTIC, which is now explained. Ions are represented by individual particles (up to 25 million total) governed by Newton's law of motion (in time units normalized to λ_{De}/c_s)

$$\frac{d\mathbf{v}}{dt} = -\nabla\phi. \quad (2)$$

The particles will be referred to as ions. Strictly speaking they are superparticles, each representing a large number of ions, but most intuitions based on regarding them as ions are physically correct. At each time-step their velocities and positions are updated (using a leapfrog scheme). Collisions possibly interrupt an ion's time-step as determined statistically. If so, the remainder of the step with the random new velocity is treated as a shortened time-step (possibly itself to be interrupted). The resulting ion density, when every ion's step is completed, is deposited on a (non-uniform, typically $32 \times 32 \times 128$) cartesian mesh of cells, and the new potential is found by solving the finite difference form of

$$\nabla^2\phi = n_e - n_i. \quad (3)$$

The system is time-stepped until it converges (up to 6000 steps of length $dt = 0.1$, though with shorter timestep during measurement periods and close to a grain). The boundary conditions used are as follows. Potential is fixed at the wall $z = 0$, periodic on the transverse (x and y) boundaries, and its gradient is fixed $d\phi/dz = \tau_c/|v_{f40}|$ at the boundary $z = 40$. The parameter v_{f40} is the flow speed at $z = 40$. It can be considered an eigenvalue. There is a self-consistent solution only for one value of v_{f40} . That value is found by iteration. For $\tau_c = 10$, it is $v_{f40} = -0.23$. [Note that a (non-ionizing) collisional sheath does not have a constant-density asymptote far from the wall. Instead it has velocity inversely proportional to a linearly rising density.]

The ions are treated as follows at the boundaries. The x and y boundaries are periodic: particles that leave are reintroduced at the opposite face. The wall just absorbs ions. None are injected there. The ions crossing the plasma boundary $z = 40$ are removed, but other ions are injected at a constant rate and with a distribution v function that represents the appropriate collisional drift distribution for the flow speed v_{f40} (and density $n_i = 1$). That distribution[16, 17] can be written

$$f_i(\mathbf{v}) = \frac{n_i}{\pi v_{tn}^2} \frac{1}{2v_f} \exp\left(-\frac{v^2}{v_{tn}^2}\right) \operatorname{erfcx}\left(\frac{v_{tn}}{2v_f} - \frac{v_z}{v_{tn}}\right), \quad (4)$$

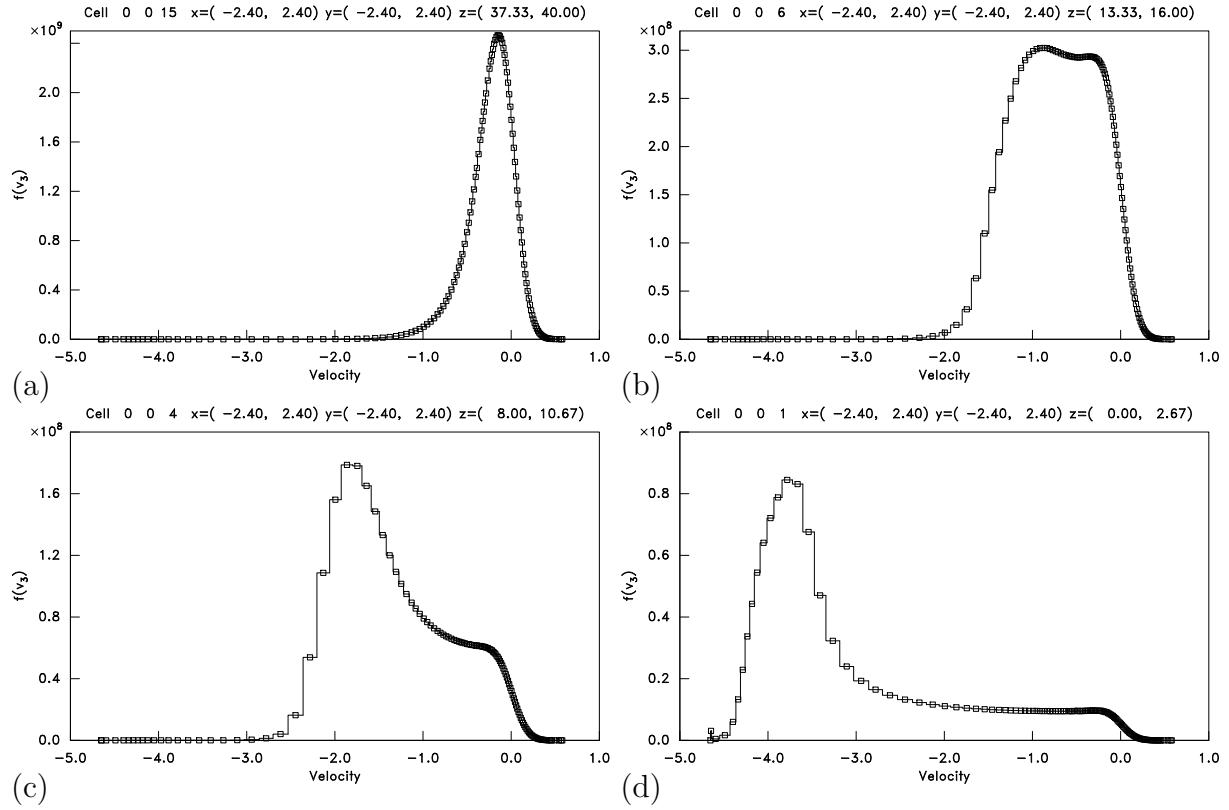


Figure 2: Ion longitudinal velocity (v_z) distribution function at four different heights. Collision time $\tau_c = 10$.

where $v_{tn} = \sqrt{2T_n/m_i}$ and $\text{erfcx}(x) \equiv \exp(x^2)\text{erfc}(x)$.

A PIC code gives, in principle, comprehensive information about the particle velocity distribution function, albeit with limitations on resolution caused by the statistical noise level. The distribution function variation with space, for the case of Fig. 1, is shown in Fig. 2. These v_z -distributions are averaged over transverse velocity and spatial position, and particles are selected only within the indicated z ranges. We see near the distant domain boundary, a typical drift distribution (a) whose shape is that of eq. (4). However, as the sheath edge is approached, strong distortion of the distribution shape occurs (b). Then passing the sheath edge the distortion forms itself into an ion beam plus a trailing plateau in velocity space towards $v_z = 0$, which is produced by collisions. This shape persists, moving deep into the sheath, with the beam becoming more pronounced and the level of the plateau decreasing.

Collision time $\tau_c = 100$ A much lower collisionality case is shown in Fig. 3. Its characteristics are similar. However, because the presheath scale, which is proportional to the mean free path, is ten times longer, it has a much larger magnitude eigenspeed: $v_{f40} = -0.83$. On

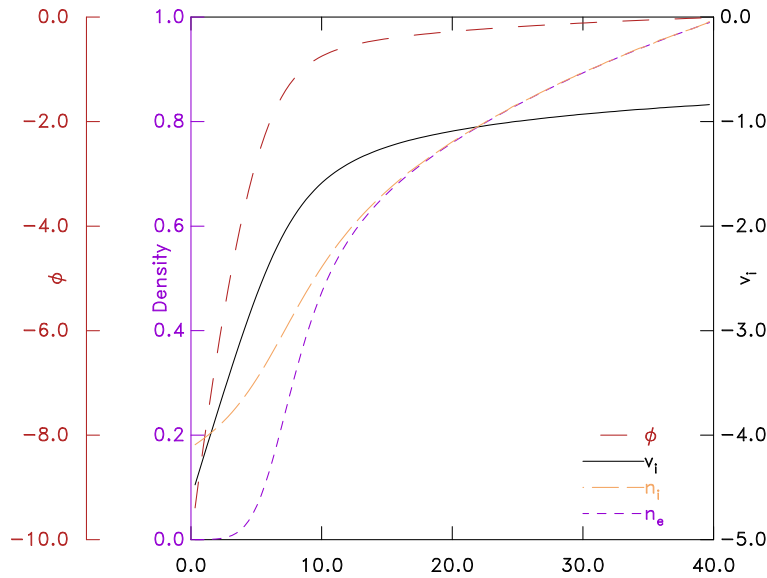


Figure 3: Sheath spatial structure for collision time $\tau_c = 100$.

the presheath scale, at $z = 40$ the solution is already close to the sheath-edge $z \approx 20$, and requires only modest acceleration to reach the sheath-edge velocity $v_f \approx -1$.

The corresponding ion velocity distributions are shown in Fig. 4. Again, at the entrance to the domain (a) the distribution is given mostly by the input particle distribution. In this case where the mean free path is longer than the domain size, there is some approximation that arises from the presumption that the particle injection is exactly the drift distribution. As the sheath edge is approached, (b), acceleration causes the distribution peak to move to higher speed, then inside the sheath, (c), a separation of the beam from zero velocity occurs, with only a tiny plateau because collisions are so infrequent. Deep into the sheath essentially all the ions are supersonic, the beam is fairly broad, but hardly any ions exist with speed

less than 2.

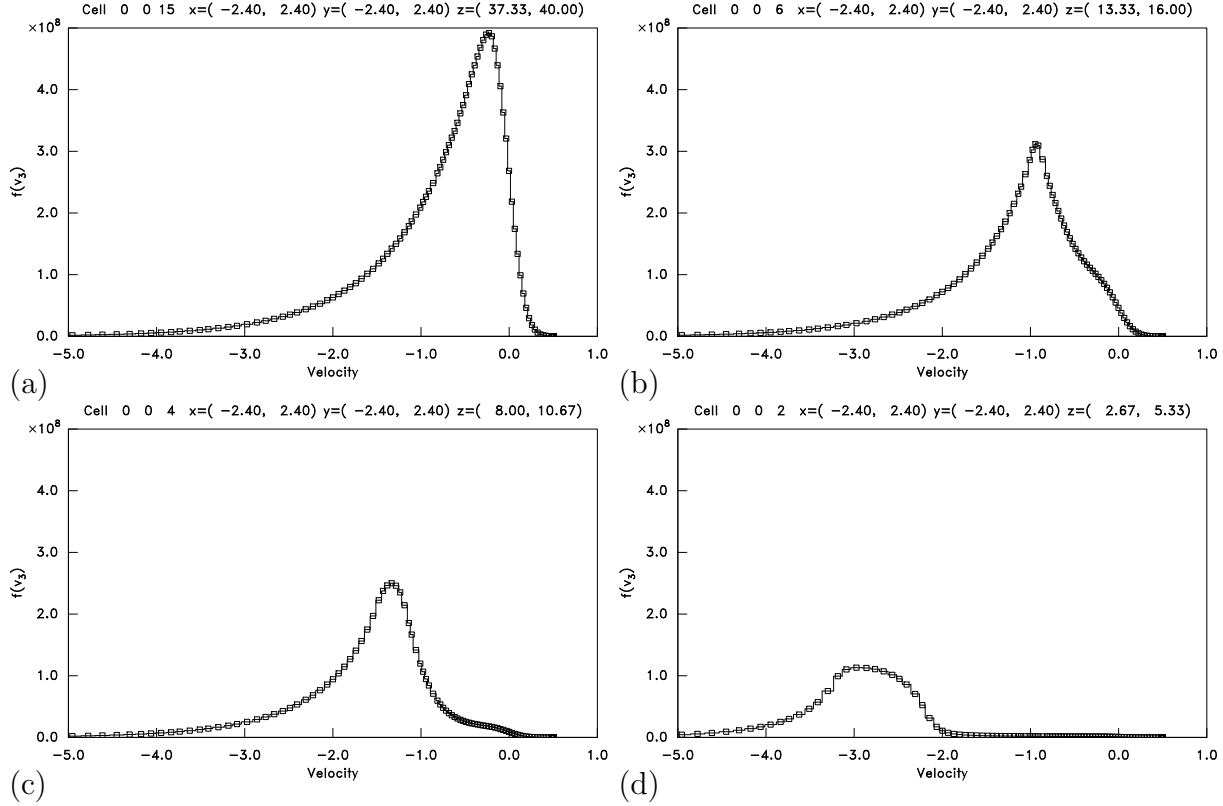


Figure 4: Ion longitudinal velocity (v_z) distribution function at four different heights. Collision time $\tau_c = 100$.

Collision time $\tau_c = 1$ A much higher collisionality case is shown in Fig. 5. There the sound-speed mean free path is 1. The eigenspeed is slow $v_{f40} = -0.035$ and the right hand boundary is deep into the presheath regime. A large drop of density occurs in the quasineutral region. It is notable that quasineutrality breaks down at position $z \approx 17$, well before the sound speed is reached. That is a reflection of there being no longer a clear distinction between sheath and presheath.

The ion distribution functions retain their collisional drift shape essentially throughout the domain, as shown in Fig. 6. That is expected since the collision length is substantially shorter than the sheath thickness.

3 Grain Force

In order to calculate the plasma force on a grain located somewhere in the sheath, COPTIC is run using all the same parameters that have given the “bare” sheath shown in the previous section, but with the addition of a grain at a chosen height (z) and centered in computational domain in the x and y directions.

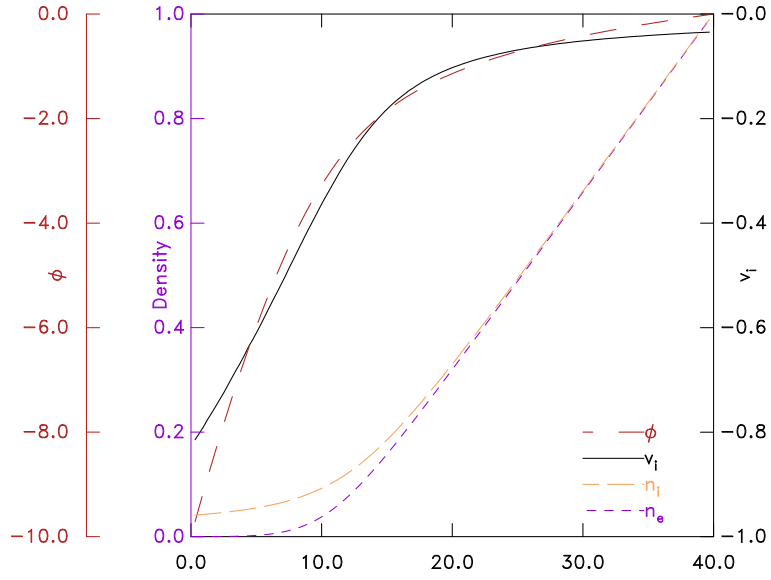


Figure 5: Collisional presheath spatial structure for collision time $\tau_c = 1$.

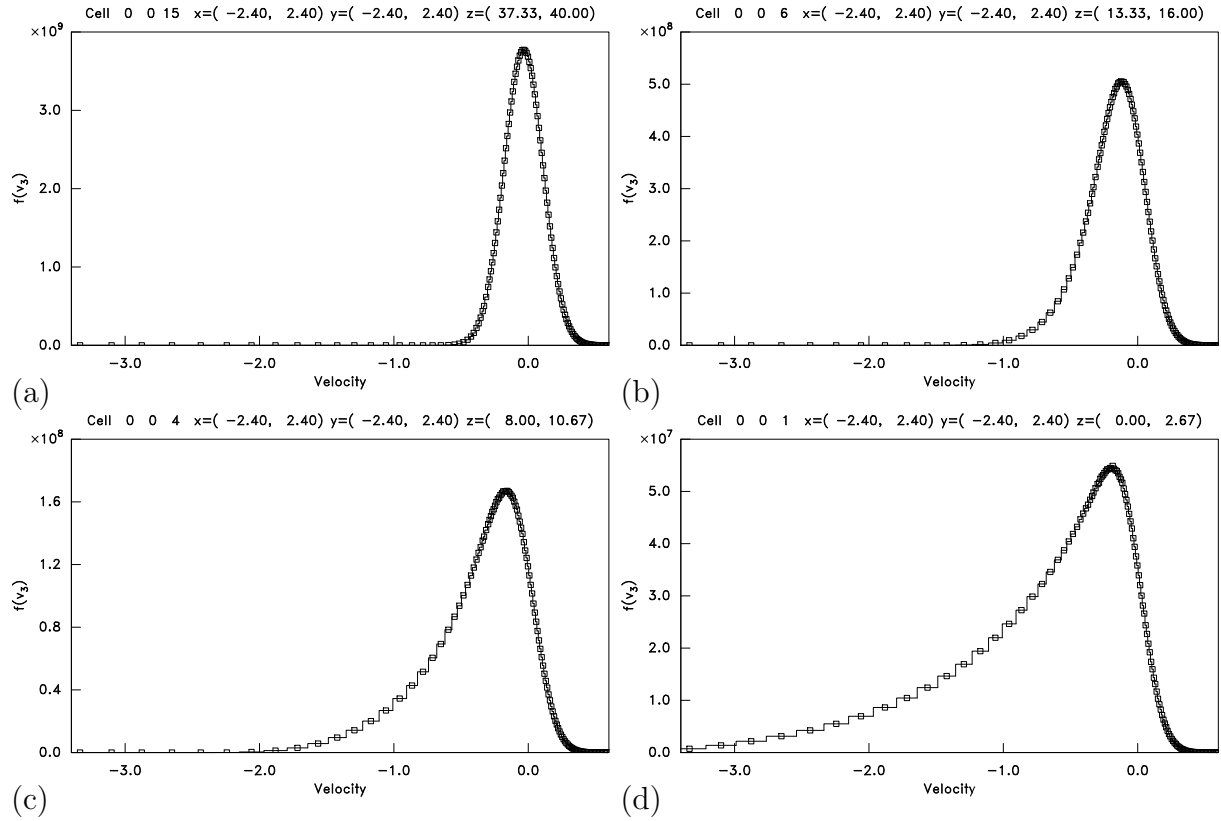


Figure 6: Ion longitudinal velocity (v_z) distribution function at four different heights. Collision time $\tau_c = 1$.

The charge on the grain, Q , is a key determining factor for the force. Generally a grain floats at a potential that is minus approximately 2 to 4 times T_e/e relative to the local potential. Denote by ϕ_p this potential *difference* between the grain surface and the local plasma potential. Moreover the capacitance of grains with radius r_p much smaller than λ_{De} is

$$C = Q/\phi_p \approx 4\pi\epsilon_0 r_p(1 + r_p/\lambda_s), \quad (5)$$

where λ_s is the shielding length. Consequently, if we define a normalized charge \bar{Q} as

$$\bar{Q} = \frac{Qe}{4\pi\epsilon_0\lambda_{De}T_e}, \quad (6)$$

then, in normalized units,

$$\bar{Q} \approx \phi_p(1 + r_p/\lambda_s)r_p. \quad (7)$$

The normalized charge \bar{Q} represents the normalized grain size times a coefficient $\phi_p(1+r_p/\lambda_s)$ that is between -2 and -4 .

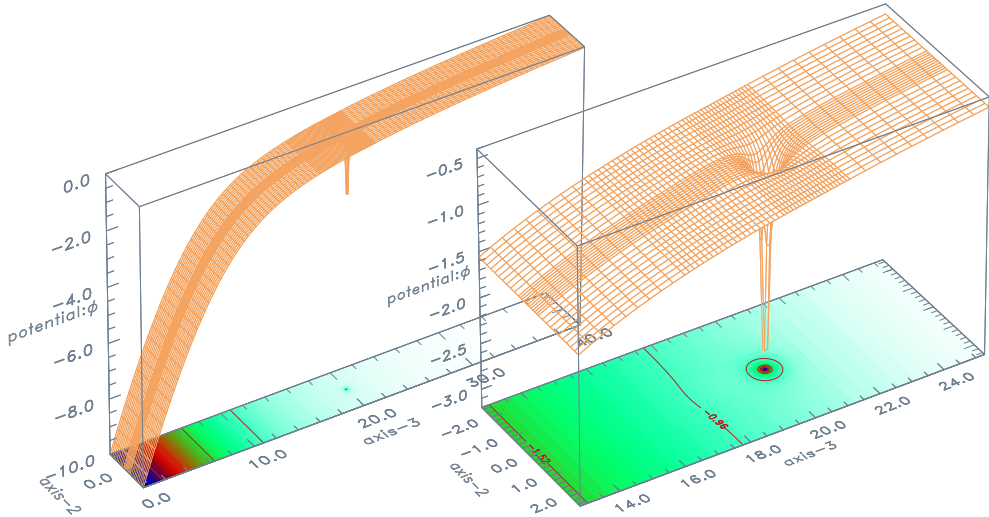


Figure 7: Example of the potential solution when a negatively charged grain is present at $z = 20$, $|\bar{Q}| = 0.02$, $\tau_c = 10$.

Fig. 7 illustrates the potential solution in the presence of a grain. The background sheath solution retains its overall form. The negative charge (at $z = 20$ in this case) causes a substantial local potential well. It is resolved, as the expanded plot illustrates, by using a local refinement of the non-uniform mesh, in the vicinity of the charge. Farther from the charge such high spatial resolution is not required, so concentrating the cells around the charge permits the simulation to avoid excessive numbers of cells overall. When the charge is placed at a different height, naturally the refinement area is moved appropriately.

Even despite this mesh refinement, a major spatial scale-length challenge remains. We are interested in grains that are much smaller than the Debye length, and simultaneously we are committed to a computational domain size that is many (40) Debye lengths in length. It remains too difficult to resolve grain radius as small as, say, 0.05 Debye lengths sufficiently well to represent the sphere. That would require a mesh spacing of say 0.01 at the grain.

The total domain would then be 4000 times longer than the smallest spacing, and computational resources would quickly be overwhelmed. So instead, a variant of the Particle-Particle Particle-Mesh (PPPM) technique[18] is used.

Within a small “analytic-radius” of the point-charge, the electric potential (and its gradient) is represented partly by an analytic potential and partly by the potential on the grid. The analytic part is equivalent to the potential of the point charge shielded by a cloud of opposite charge whose density is proportional to radius. The cloud extends out to the analytic-radius where the point-charge is fully shielded; the analytic field is zero outside the analytic-radius. The rest of the potential is represented on the grid. It is found by solving Poisson’s equation discretely. Incidentally, the plots of Fig. 7 are of the *total* equivalent potential, i.e. the sum of the discretely represented potential plus the value of the analytic potential at the grid points. This PPPM technique means it is not necessary for the grid to resolve the potential very close to the grain-center because it is mostly represented there by the analytic form. Outside of the analytic-radius it is fully represented on the grid and the analytic form is zero. In this work the analytic-radius is chosen as $0.4(\lambda_{De})$. The grid spacing near the grain is ~ 0.1 . For each run, \bar{Q} is specified — a fixed grain charge.

The grain is also surrounded by a “grain-sphere”, of radius equal to the grain radius, in which no plasma is present. Ions that enter the grain-sphere are removed from the simulation. The radius of the grain-sphere, r_p , is chosen in accordance with eq. 7 (ignoring r_p/λ_s), as

$$r_p = \bar{Q}/\phi_p = -0.5\bar{Q}. \quad (8)$$

In other words, the grain size is chosen consistent with grain surface potential of $-2T_e/e$. For given \bar{Q} the precise grain-sphere radius has only a fractionally smaller effect on total grain force.

The force on the grain is obtained from the final steady solution by placing around it three reference spheres of radius 0.5, 0.8, and 1.0. The total momentum flux inward across each of the reference spheres is measured in the code from the sum of Maxwell stress, electron pressure, and ion momentum flux[19, 16]. The total collisional momentum loss (to neutrals) within each sphere is subtracted, and in steady state the remainder is the momentum flux to the grain. Any discrepancies between the grain momentum flux calculated from the different spheres represents the uncertainty in the calculation, since an exact calculation should be independent of reference sphere radius.

A code run of 2000 steps starting from the corresponding bare sheath conditions is generally well converged for the second half of its duration. The average z -force during that period is found. Transverse force components are observed to be zero to high precision, as expected from symmetry. Many such runs are carried out to scan different heights and different normalized charge values.

Fig. 8 shows the results for the moderate collisionality case $\tau_c = 10$. The force measured and plotted is the total plasma force, which includes the effect of the background electric potential gradient acting on the charge, as well as the ion drag force arising from the plasma flow past the charge. It is in units of $n_e T_e \lambda_{De}^2$, but normalized by dividing by $|\bar{Q}|$. The background electric field force ($-Q\nabla\phi$ using the bare sheath potential), normalized in this way, is therefore independent of $|\bar{Q}|$. Its value is indicated by short horizontal lines at the left of the plot, separated by a gap from the full plasma force data. In a collisionless situation,

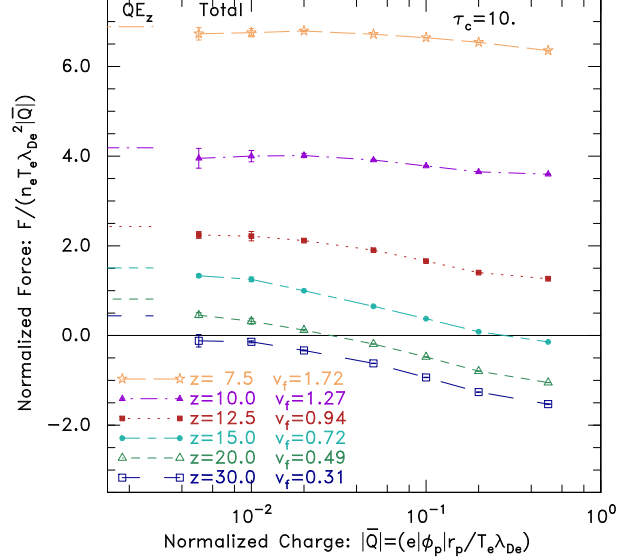


Figure 8: Normalized total plasma force as a function of normalized charge, for various different heights in a sheath with collision time $\tau_c = 10$.

the normalized ion drag force at small $|\bar{Q}|$ is proportional to $|\bar{Q}|$. Therefore one expects the limit of the total force at small $|\bar{Q}|$ to equal simply the background electric field force. We do not actually proceed to the limit, because the force becomes increasingly difficult to measure and subject to uncertainties at low $|\bar{Q}|$. However, the plot appears to confirm the expectation.

One way to use the data of this plot is to suppose that the non-plasma forces (e.g. gravity) are known; and then find the place where a grain of a certain charge is in equilibrium with total force equal zero. If non-plasma forces are zero, for example, then equilibrium is at Force per charge = 0. A grain at $z = 20$ is then in equilibrium if it has a charge of just under $|\bar{Q}| = 0.05$; a grain of charge $|\bar{Q}| = 0.2$ will float at $z \approx 15$; and so on.

Fig. 9 shows force results for the low, (a) $\tau_c = 100$, and high, (b) $\tau_c = 1$, collisionality sheaths. As before the force is mostly electric field force at the left hand, low $|\bar{Q}|$, side of the plot. The predominant differences are due to the altered potential and velocity profiles. It is notable that the variation of force with $|\bar{Q}|$ is substantially less for the high-collisionality sheath and the force is positive even above $z = 20$. If non-plasma forces were negligible for that case, a grain would float high above the sheath at a position where the flow speed is smaller than $0.1c_s$ (see Fig. 5). One should be cautious in situations with strong collisionality about making the naive assumption that the flow at the grain is necessarily sonic. By contrast, at low collisionality, $\tau_c = 100$, even gravitationless grains don't float above $z = 20$, and the speed is indeed essentially equal to c_s or greater (see Fig. 3) at that height or below.

4 Comparison with Uniform-Plasma Force

The observed force values are now compared in detail with the force that would be predicted for a uniform-plasma with appropriate conditions.

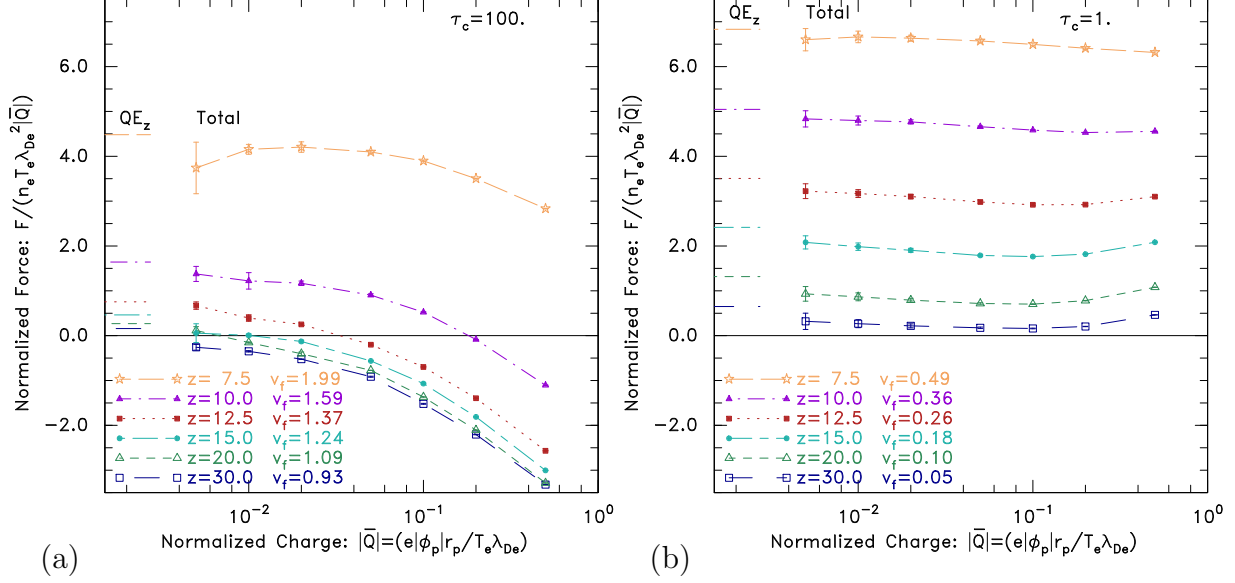


Figure 9: Normalized force for collision times (a) $\tau_c = 100$ and (b) $\tau_c = 1$.

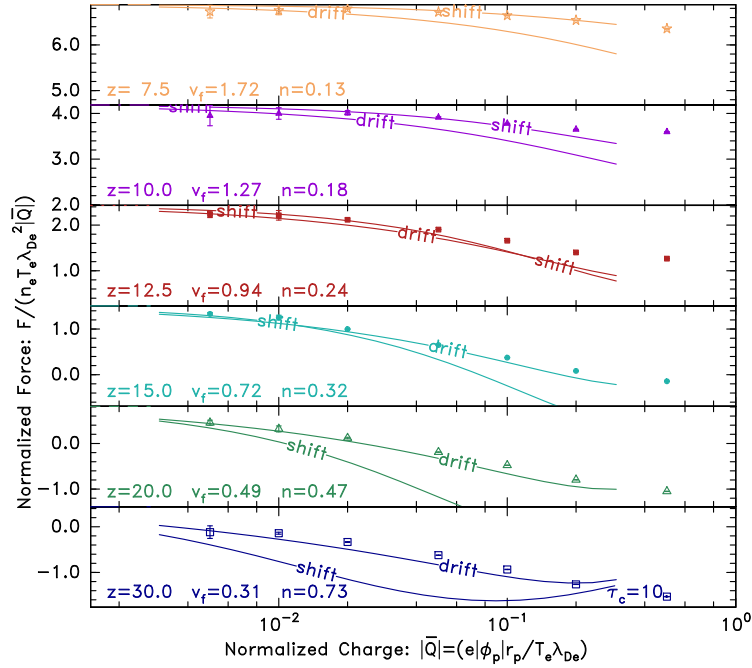


Figure 10: Comparison of force derived from COPTIC with a combination of the background electric field force and the fitted ion drag force[20]. Moderate collisionality $\tau_c = 10$. The solid lines are theory for a *shifted* Maxwellian and the *drift* distribution [eq. 4].

For each position z the value of the density n_i , flow velocity v_f , and electric field $-\nabla\phi$ are obtained from the data of section 2, i.e. the bare sheath, for the appropriate value of the collisionality. The ion drag force for a uniform plasma with that density and velocity is obtained from the fitted analytic approximations to computational evaluations of the drag force, recently published[20]. Details are summarized in the appendix. The value of the Debye length used in the analytic force is equal to the reference value (1) divided by the square-root of the local normalized density (at z , relative to the reference density at $z = 40$); and the analytic force is multiplied by the local normalized density to render it into the units normalized to the reference density.

The analytic drag force (which is negative) is added to the (positive) electric field force given by the grain charge multiplied by the background electric field. The result is the predicted total uniform-plasma force for a grain residing in a plasma whose properties are those of a bare sheath at the position of the grain. However, notice that the electric field is *not* exactly the same as it would be in a uniform plasma. In a plasma in which the ion flow arises from a flow of background neutrals — the “shift” case with shifted Maxwellian ion distribution — there would be zero electric field. In a uniform plasma where the ion flow is driven by an electric field, the distribution takes the “drift” form and the electric field is directly related to the flow velocity through $-\nabla\phi = v_f/\tau_c$ (in normalized units). In neither case is the uniform-plasma electric field exactly equal to that in the bare sheath, because even in the drift case, ion acceleration in the sheath is part of the net average force balance, causing the bare-sheath electric field to deviate from v_f/τ_c . This difference in electric field means that the uniform-plasma ion drag prediction cannot be expected to be exactly equal to the drag in a non-uniform sheath.

In Fig. 10 are shown the COPTIC data compared with the analytic predictions, for the moderate collisionality case. The upper boundary of each frame is placed at the value of the electric field force. The analytic fits for drift distributions are not validated for $r_p/\lambda_{De} > 0.1$, which corresponds to $|\bar{Q}| > 0.2$, so the fit lines are not extended to the maximum COPTIC point at $|\bar{Q}| > 0.5$. Two fit lines are shown, corresponding respectively to the drift or shift distributions (with specified v_f). We observe that for distant points such as $z = 30, 20, 15$, the *drift* curve fits the COPTIC data rather well, whereas the *shift* curve does not. The observed distribution function in this height range is much better approximated by the drift distribution, as seen in Fig. 2. However, as the height decreases $z = 10, 7.5$, into the sheath the ions accelerate so as to adopt a more “beam-like” distribution (Fig. 2c). The corresponding force then agrees better with the shift analytic expression.

In all cases, as the charge becomes small, the values appear to be approaching the electric-field value. However, the force uncertainty estimated from the difference between the values measured by different spheres, eventually becomes significant. Recall that the plot is of the force divided by \bar{Q} , so absolute uncertainty is magnified at low $|\bar{Q}|$ in the normalized force. We therefore do not explore below $|\bar{Q}| = 0.005$.

Fig. 11 shows the same comparison for the low collisionality sheath $\tau_c = 100$. It shows much the same trend of a transition between drift- and shift-like distributions and forces; although the predicted differences between the forces are somewhat smaller in this case.

Fig. 12 shows the comparison for the high-collisionality case, $\tau_c = 1$. We know from Fig. 6 that for this case the bare sheath shows drift-like distributions throughout the range of z . Accordingly, the drift-force prediction agrees substantially better than the shift-force, at all

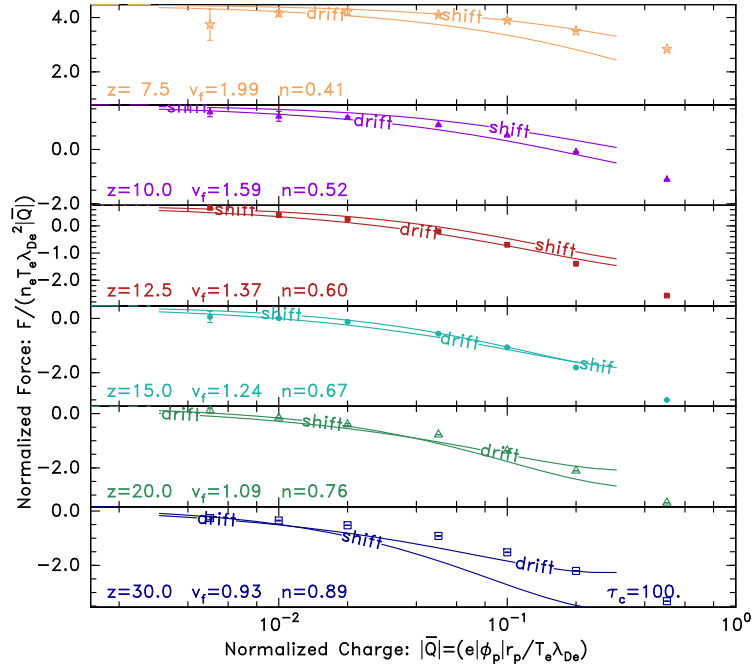


Figure 11: As for Fig. 10 except for low collisionality $\tau_c = 100$.

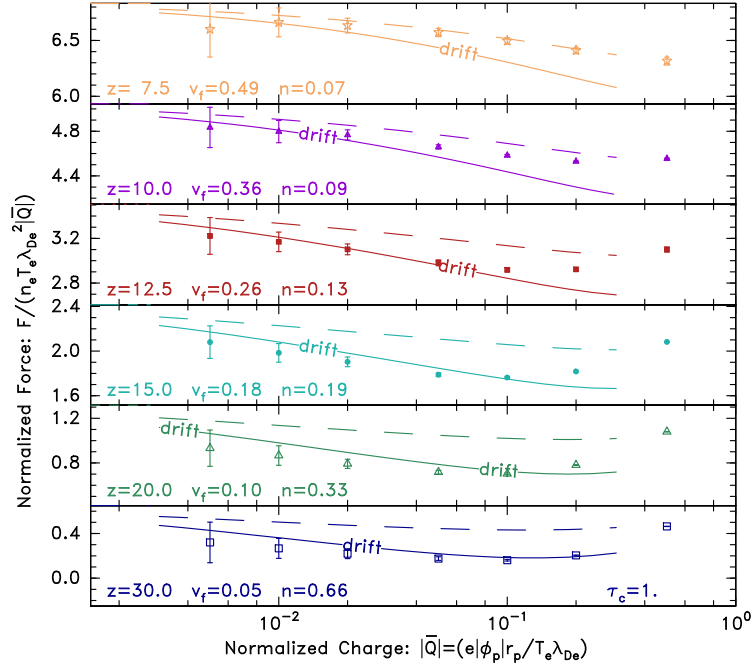


Figure 12: Comparison of force derived from COPTIC with a combination of the background electric field force and the ion drag force including (solid line) or excluding (dashed line) the collisional force factor[20]. High collisionality $\tau_c = 1$.

positions. No shift-force predictions are plotted. Instead, in addition to the full drift-force prediction, the low-collisionality drift-distribution force is shown as a dashed line. Its drag component is approximately a factor of two less than the full prediction because as has been documented[20] there is a factor of two enhancement of the drift force directly by collisions at collisionalities like this. We therefore see that it is necessary to include the collisional force enhancement in order to obtain agreement with COPTIC’s observed forces.

Significant disagreement remains, however, for the larger charges, $|\bar{Q}| \gtrsim 0.1$. In addition to the inexactness of the comparisons for reasons already explained, another important effect has been observed. It is that, for large charges at high collisionality, an extended Coulomb-like (rather than Yukawa-like) potential well appears. The $1/r^2$ potential gradient is necessary in order to draw the ion flux to the absorbing grain through the collisional plasma, see e.g.[21]. The plasma density, potential, and velocity as a whole are then substantially perturbed by the presence of the grain, as illustrated by Fig. 13. Notice that the density at the ($z = 40$) edge of the computational domain (Fig. 13(a)) has dropped below unity because of the presence of the charge. This effect is reduced by using a wider domain

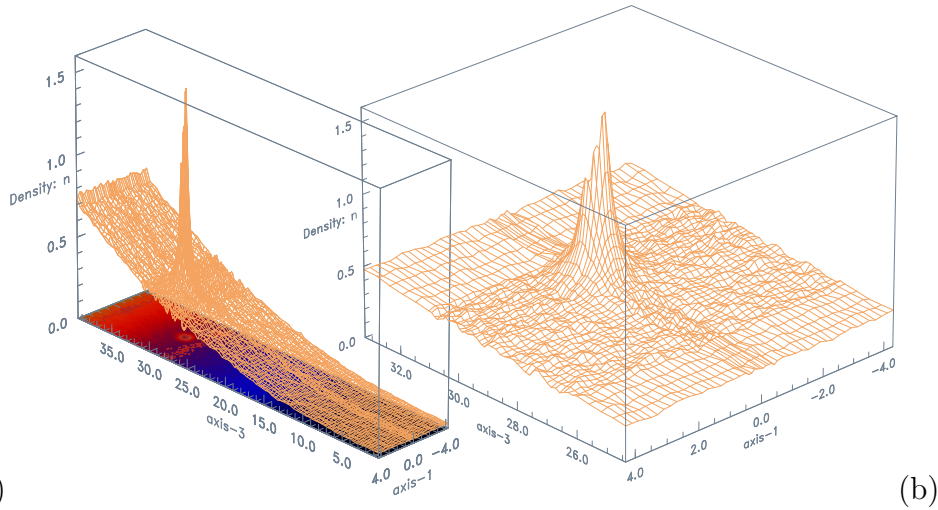


Figure 13: Illustration of the strong perturbation of the sheath density by a large charge. $|\bar{Q}| = 0.05$, in the high collisionality case $\tau_c = 1$. (a) Entire domain. (b) Vicinity of charge.

$(9\lambda_{De}, 52 \times 52 \times 128)$, which indicates that it arises from the proximity of “mirror” charges in the array represented by the periodic boundary conditions. The wider domain is used for these high collisionality cases for $|\bar{Q}| \geq 0.05$, below which the effect is negligible. Even so, the largest charges, such as shown in Fig. 13, remain substantially affected. This is the main reason for the upturn of the COPTIC force and the disagreement with the analytic theory applied to the unperturbed sheath parameters. Computational cost increases proportional to the square of the domain width; so the calculations have not been pursued to domains wide enough to remove perturbation at the highest charge.

5 Application

In order to use the dimensionless force information provided here, either that plasma force must be translated into dimensional units or the other forces into dimensionless form. This can be done by realizing that the unit of force used here is

$$F_u = n_e T_e \lambda_{De}^2 = \epsilon_0 (T_e/e)^2 = 8.85 \times 10^{-12} T_{eV}^2, \quad (9)$$

where T_{eV} is the electron temperature in electron Volts. The normalized charge (see eq. (8)) in dimensional units is (to lowest order in r_p/λ_{De})

$$|\bar{Q}| = (e|\phi_p|/T_e)(r_p/\lambda_{De}). \quad (10)$$

Consequently the force normalization is

$$F_u |\bar{Q}| = \epsilon_0 T_{eV}^2 (|\phi_p|/T_{eV})(r_p/\lambda_{De}). \quad (11)$$

To express a gravitational force conveniently in normalized units, suppose that the grain density is ρ_g g/cm³, the acceleration due to gravity is $g = 9.8$ m/s², and let λ_{mm} denote λ_{De} measured in mm, and r_μ denote r_p measured in μ m. Then the force due to gravity expressed in units of $F_u |\bar{Q}|$ is

$$\bar{F}_g = \frac{(4\pi/3)r_p^3 \rho_g}{\epsilon_0 T_{eV}^2 (|\phi_p|/T_{eV})(r_p/\lambda_{De})} = 4.63 \frac{\rho_g \lambda_{mm} r_\mu^2}{T_{eV}^2 (|\phi_p|/T_{eV})}. \quad (12)$$

For example, if we consider typical dusty plasma parameters: $\rho_g = 1.5$ (melamine formaldehyde); $T_{eV} = 2$; $\lambda_{mm} = 0.5$; $|\phi_p|/T_{eV} = 2$; $r_\mu = 3$; we get $\bar{F}_g = 3.9$. This grain has $\bar{Q} = 1.2 \times 10^{-2}$ and the dominant plasma force is the background electric field. In argon the charge-exchange mean-free-path ℓ_c (mm) and neutral pressure p_n (Pa) are related approximately by $\ell_c p_n \approx 6$, which determines the neutral pressure corresponding to each collisionality. There is thus an equilibrium between gravity and plasma force at approximately the parameters of Table 1.

τ_c	p_n	z/λ_{De}	$ v_f /c_s$	n_i/n_{40}
1	10	12	0.3	0.1
10	1	10	1.3	0.2
100	0.1	8	1.9	0.4

Table 1: Gravitational equilibrium values for the example case under three different collisionality levels.

When the gravitational force is lower, either because the gravitational acceleration g is decreased in microgravity environments, or because the mass density is lower for hollow spheres, then the ion drag force becomes a more important fraction of the equilibrium, and larger values of $|\bar{Q}|$ become important.

In summary, self-consistent one-dimensional kinetic calculations of the DC collisional sheath have been carried out and show complicated changes in the ion distribution function.

The plasma force on a spherical grain of specified charge in the sheath has been found by direct PIC simulation. It agrees quite well with the combination of background electric field force and ion drag force. However, differences in the drag force as much as a factor of two arise from differences in the ion velocity distribution function. So, quantitative agreement requires use of non-Maxwellian drift distribution in most cases, not a shifted Maxwellian. The direct enhancement of the drag force by collisions is also observed in strongly collisional cases.

Acknowledgments

Useful discussions with C B Haakonsen are gratefully acknowledged. Work supported in part by NSF/DOE Grant DE-FG02-06ER54982. Some of the computer simulations were carried out on the MIT PSFC parallel AMD Opteron/Infiniband cluster Loki.

Appendix: Drag force expressions

This appendix specifies the analytic theoretical form of drag force used to compare with the present calculations. Code to evaluate it is available accompanying reference [20].

The drag force is written as the sum of an orbital part F_o and a direct collection part F_c corrected by a collisional force factor \bar{F} equal to 1 at low collisionality; so $F = \bar{F}(F_o + F_c)$. The orbital part is

$$F_o = n_e T_e r_p^2 \left(\frac{e\phi_p}{T_e} \right)^2 \frac{T_e}{T_i} 4\pi G(u_f) \ln \Lambda, \quad (13)$$

where u_f is the flow velocity normalized to the ion thermal speed $\sqrt{2T_i/m_i}$.

For the *shift* distribution the function $G(u_f)$ is simply the Chandrasekhar function

$$G_s(u) \equiv \left[\text{erf}(u) - 2ue^{-u^2}/\sqrt{\pi} \right] / (2u^2). \quad (14)$$

$$\ln \Lambda_s = \ln \left(\frac{b_{90} + \lambda_\ell}{b_{90} + r_p} \right), \quad (15)$$

$$b_{90s} = e\phi_p / (2T_i + \mathcal{E}_s), \quad (16)$$

where

$$\mathcal{E}_s = 0.5m_i v_f^2 \left[1 + |v_f/0.4c_s|^3 \right] \quad (17)$$

represents the effects of flow. And

$$\lambda_\ell^2 = r_p^2 + \lambda_{De}^2 [1 + T_e / (T_i + \mathcal{E}_s)]. \quad (18)$$

For the *drift* case,

$$G_d(u) = u / (2.66 + 1.82u^2), \quad (19)$$

$$\ln \Lambda_d = \ln \left(\frac{b_{90d} + \lambda}{b_{90d} + 1.5r_p} \right), \quad (20)$$

$$b_{90d} = e\phi_p / [T_i + \sqrt{100T_i T_e r_p / \lambda_{De}} v_f^2 / (c_s^2 + 2.5v_f^2)], \quad (21)$$

where

$$r_c = \left(\frac{|Q|e}{4\pi\epsilon_0 T_e r_p} \right)^{\frac{1}{5}} \left(\frac{5\sqrt{\pi}}{8} \right)^{\frac{2}{5}} \left(\frac{r_p T_i}{\lambda_{De} T_e} \right)^{\frac{1}{5}} \lambda_{De}, \quad (22)$$

$$\lambda^{-2} = \lambda_{De}^{-2} + (r_c^2 + \lambda_{De}^2 \sqrt{T_i/T_e} v_f/c_s)^{-1}. \quad (23)$$

The collection force for the shift distribution is

$$F_{cs}(u_f) = n_i T_i r_p^2 2\pi \{u_f^2 + (1 + \chi)[1 - (1 + bu_f)e^{-au_f}]\} \quad (24)$$

where $b = 0.8$,

$$a = b + \frac{(16 + 8\chi)}{6\sqrt{\pi}(1 + \chi)} \quad (25)$$

and $\chi \equiv -e\phi_p/T_i$ is potential normalized to ion temperature. For the drift distribution the collection force is

$$F_{cd}(u_f) = n_i r_p^2 T_i 2\pi \left[2u_f^2 + (1 + \chi) \frac{(a - b)u_f + (au_f)^2}{(1 + au_f)^2} \right]. \quad (26)$$

The collisional correction factor is a function only of $\bar{v} = r_c/\tau_c c_s$:

$$\bar{F}(\bar{v}) = \frac{1 + c\bar{v}}{1 + d\bar{v} + e\bar{v}^2} \quad (27)$$

in which the coefficients are given by Table 2.

Case	c	d	e
Drift	$(7 + 30v_f/c_s)$	$18v_f/c_s$	$0.5c$
Shift	5	$8v_f/c_s$	3.2

Table 2: Coefficients for the shift and drift cases of eq. (27).

References

- [1] A Melzer, T Trottenberg, and A Piel. Experimental determination of the charge on dust particles forming Coulomb lattices. *Physics Letters A*, 191:301–308, 1994.
- [2] G A Hebner and M E Riley. Measurement of attractive interactions produced by the ion wakefield in dusty plasmas using a constrained collision geometry. *Phys. Rev. E*, 68:46401, 2003.
- [3] A A Samarian, S. V. Vladimirov, and B. W. James. Dust particle alignments and confinement in a radio frequency sheath. *Physics of Plasmas*, 12(2):022103, 2005.
- [4] V Fortov, A Ivlev, S Khrapak, A Khrapak, and G Morfill. Complex (dusty) plasmas: Current status, open issues, perspectives. *Physics Reports*, 421(1-2):1–103, December 2005.

- [5] K-U Riemann. The Bohm criterion and sheath formation. *Journal of Physics D: Applied Physics*, 24:493, 1991.
- [6] K-U Riemann. Kinetic analysis of the collisional plasmashath transition. *Journal of Physics D: Applied Physics*, 36(22):2811–2820, November 2003.
- [7] K.-U. Riemann. Kinetic theory of the plasma sheath transition in a weakly ionized plasma. *Physics of Fluids*, 24(12):2163, 1981.
- [8] Aleksey Vasenkov and Bernie Shizgal. Self-consistent kinetic theory of a plasma sheath. *Physical Review E*, 65(4):046404, March 2002.
- [9] N. Jelic, K.-U. Riemann, T. Gyergyek, S. Kuhn, M. Stanojevic, and J. Duhovnik. Fluid and kinetic parameters near the plasma-sheath boundary for finite Debye lengths. *Physics of Plasmas*, 14(10):103506, 2007.
- [10] I H Hutchinson. Nonlinear collisionless plasma wakes of small particles. *Phys. Plasmas*, 18:32111, 2011.
- [11] I H Hutchinson. Forces on a Small Grain in the Nonlinear Plasma Wake of Another. *Physical Review Letters*, 107(9):2–5, August 2011.
- [12] I H Hutchinson. *Principles of Plasma Diagnostics*. Cambridge University Press, Cambridge, UK, first edition, 1987.
- [13] T Nitter. Levitation of dust in rf and dc glow discharges. *Plasma Sources Science and Technology*, 5:93, 1996.
- [14] V R Ikkurthi, K Matyash, A Melzer, and R Schneider. Computation of charge and ion drag force on multiple static spherical dust grains immersed in rf discharges. *Phys. Plasmas*, 17:103712, 2010.
- [15] André Melzer, Simon Hübner, Lars Lewerentz, Konstantin Matyash, Ralf Schneider, and Ramana Ikkurthi. Phase-resolved optical emission of dusty rf discharges: Experiment and simulation. *Physical Review E*, 83(3):036411, March 2011.
- [16] Leonardo Patacchini and Ian H Hutchinson. Fully Self-Consistent Ion-Drag-Force Calculations for Dust in Collisional Plasmas with an External Electric Field. *Physical Review Letters*, 101(2):1–4, July 2008.
- [17] M. Lampe, T. B. Rucker, G. Joyce, S. K. Zhdanov, A. V. Ivlev, and G. E. Morfill. Ion distribution function in a plasma with uniform electric field. *Physics of Plasmas*, 19(11):113703, 2012.
- [18] R W Hockney and J W Eastwood. *Computer Simulation using Particles*. Taylor and Francis, London, 1988.
- [19] I H Hutchinson. Ion collection by a sphere in a flowing plasma: 3. Floating potential and drag force. *Plasma Physics and Controlled Fusion*, 47(1):71–87, January 2005.

- [20] I H Hutchinson and C B Haakonsen. Collisional Effects on Nonlinear Ion Drag Force for Small Grains. *Physics of Plasmas*, 20:083701, 2013.
- [21] C H Su and S H Lam. Continuum theory of spherical electrostatic probes. *Physics of Fluids*, 6:1479–1491, 1963.